Solar Energy 206 (2020) 555–563

Contents lists available at ScienceDirect

Solar Energy

journal homepage: www.elsevier.com/locate/solener

Effect of Na and the back contact on $Cu_2Zn(Sn,Ge)Se_4$ thin-film solar cells: Towards semi-transparent solar cells

Andrea Ruiz-Perona[a], Yudania Sánchez[b], Maxim Guc[b], Samira Khelifi[c], Tim Kodalle[d], Marcel Placidi[b], José Manuel Merino[a], Máximo León[a], Raquel Caballero[a,*]

[a] Universidad Autónoma de Madrid, Departamento de Física Aplicada, C/ Francisco Tomás y Valiente 7, 28049 Madrid, Spain
[b] IREC, Catalonia Institute for Energy Research, C/ Jardins de les Dones de Negre 1, Sant Adriá del Besòs, 08930 Barcelona, Spain
[c] Department of Solid State Sciences, Ghent University, Krijgslaan 281-S1, 9000 Ghent, Belgium
[d] PVcomB, Helmholtz-Zentrum Berlin für Materialien und Energie, Schwarzschildstraße 3, 12489 Berlin, Germany

ARTICLE INFO

Keywords:
Kesterite
Solar cells
Na
Ge
Semi-transparent
FTO

ABSTRACT

$Cu_2ZnSn_{1-x}Ge_xSe_4$ (CZTGSe) thin films have been grown onto Mo/SLG and Mo/V_2O_5/FTO/SLG substrates using thermal co-evaporation followed by a subsequent thermal annealing. A NaF precursor layer was evaporated prior to the deposition of the kesterite absorber layer. In the samples grown on Mo/SLG, it has been found that Na promotes Ge incorporation into the $Cu_2ZnSnSe_4$ lattice. The high concentration of incorporated Ge leads to the segregation of Sn-Se secondary phases as well as to an accumulation of Sn next to the Mo layer. The use of 12 and 16 nm NaF thick precursor layers prior to the CZTGSe deposition leads to absorber band gaps of 1.30 and 1.34 eV, and to device performances of 4.7 and 4.0%, respectively. A higher Na content, furthermore, caused the formation of bigger grains, a higher charge carrier concentration and a shorter depletion width. A 12 nm NaF precursor layer was used for the devices grown on FTO-based substrates, producing an optimal back contact that allows achieving efficiencies of 5.6% and transmittance of 30% in the near infrared range. This enhanced performance can be associated with the absence of secondary phases and Ge distribution through the absorber layer. The formation of a $MoSe_2$ layer at the back interface in all the investigated devices seems to play a crucial role to improve the solar cell efficiency.

1. Introduction

The kesterite $Cu_2ZnSn(S,Se)_4$ (CZTSSe) is an attractive material for absorber layer in thin film solar cells because of its low toxicity and earth's abundant nature. However, so far, efficiencies of kesterite-based devices are limited to around 12.6% (Wang et al., 2014; Son et al., 2019). The main limitation of this technology is the rather high open circuit voltage deficit (E_g/q - V_{OC}), which has been attributed to different factors such as the presence of secondary phases, the non-optimal quality of the kesterite absorber layers, the unfavorable alignment of the conduction band minimum at the heterointerface, etc. (Platzer-Björkman et al., 2015; Giraldo et al., 2019). Improvements of the V_{OC}-deficit and the optoelectronic properties of kesterite have been reported with Ge incorporation (Giraldo et al., 2019; Kim et al., 2016). It is also well known that the band-gap energy of the absorber layer can be tuned by partial or total substitution of Sn with Ge, between 1.0 eV ($Cu_2ZnSnSe_4$, CZTSe) and 1.4 eV ($Cu_2ZnGeSe_4$, CZGSe) (Kim et al., 2016). Wide band-gap absorber layers are attractive for top cells of a cost-efficient tandem device, but also for semi-transparent solar cells for efficient and stable advanced Building Integrated Photovoltaic (BIPV) concepts (Espíndola-Rodríguez et al., 2017; Ge et al., 2015).

Most of the kesterite-based solar cells use Mo as back contact because of its good ohmic behavior through the formation of a $Mo(S,Se)_2$ layer at the back interface, its thermal stability, etc. (Temgoua et al., 2019). However, many applications, for which wide band-gap absorber compounds compete with other more mature technologies, require a transparent back contact. For these applications, as e.g. the fabrication of bifacial and semi-transparent photovoltaic devices, the use of a transparent conductive oxide (TCO) layer as a back contact is necessary (Espíndola-Rodríguez et al., 2017; Ge et al., 2015; Temgoua et al., 2019). Tin doped indium oxide, In_2O_3:SnO_2 (ITO) and fluorine doped tin oxide, SnO_2:F (FTO) are the most common TCOs used for this purpose. Up to now, better kesterite-based solar cells have been produced by using FTO as back contact. The poor performance of devices with an ITO back contact was attributed to In diffusion into the CZTSSe layer and the formation of SnO_x (Ge et al., 2015). However, Temgoua et al.

* Corresponding author.
E-mail address: raquel.caballero@uam.es (R. Caballero).

https://doi.org/10.1016/j.solener.2020.06.044
Received 17 April 2020; Received in revised form 8 June 2020; Accepted 10 June 2020
Available online 17 June 2020

Table 1
Composition of $Cu_2Zn(Sn,Ge)Se_4$ thin films measured by EDX.

Sample	NaF (nm)	[Cu] (at%)	[Zn] (at%)	[Sn] (at%)	[Ge] (at%)	[Se] (at%)	[Cu]/([Zn] + IV)	[Zn]/IV	[Ge]/IV	[Se]/M
Ref.	0	23.1	13.3	6.2	6.7	50.7	0.88	1.02	0.52	1.03
1	12	21.2	14.6	3.8	7.8	52.6	0.81	1.26	0.67	1.11
2	16	20.3	14.8	4.1	9.2	51.2	0.72	1.11	0.69	1.06
3	12	21.5	13.4	5.0	7.8	52.3	0.82	1.05	0.61	1.10

Note: IV = [Ge] + [Sn]; M = [Cu] + [Zn] + [Sn] + [Ge].

(Temgoua et al., 2019) demonstrated that FTO is quite stable under Se atmosphere even at 600 °C. Although an ohmic contact between CZTSe and FTO is achieved, a higher series resistance is obtained than in case of CZTSe deposited on a Mo back contact. An important efficiency enhancement of CZTSe and CZTSSe-based devices fabricated onto FTO/SLG was achieved when a 20 nm Mo layer was deposited onto a FTO/SLG substrate (Espíndola-Rodríguez et al., 2017). Another possibility to enhance the back interface of kesterite-based devices is the inclusion of a thin layer of a transition metal oxide to act as hole extractor. Different groups have reported an improvement of the back interface and the final solar cell efficiency using a thin layer of MoO_x (López-Marino et al., 2016; Liu et al., 2018). Other metal oxides have been used for different technologies, as for example, V_2O_5 has been shown to be a potential candidate for the use as hole selective contact in silicon heterojunction solar cells (Almora et al., 2017).

Another option that has been explored to enhance the efficiency of kesterite-solar cells is the incorporation of Na into the absorber layer (Repins et al., 2012; Li et al., 2013; Xie et al., 2016; Sutter-Fella et al., 2014; Abzieher et al., 2016; Andres et al., 2018). Neuschitzer et al. (2016) reported an interaction of Ge and Na in Ge-doped $Cu_2ZnSnSe_4$ (CZTSe) absorber layers, which minimizes the loss of Sn and the formation of secondary phases, leading to enhanced device performance. Na, the most investigated alkali element, diffuses through the Mo layer into the kesterite film when soda-lime glass (SLG) is used as a substrate. However, the TCO layer blocks the Na diffusion towards the absorber, being detrimental for the solar cell efficiency. Therefore, it is necessary to add Na in a controlled way that allows improving the absorber-properties and device performance (Caballero et al., 2006; Espíndola-Rodríguez et al., 2017). Espíndola-Rodríguez et al. (2017) demonstrated that an intermediate Mo or Mo:Na nanolayer between FTO and the CZTSSe absorber film improved the back electrode performance characteristics of kesterite solar cells without a significant loss of the FTO transparency. The combination of the positive effect of Na and the use of a Mo layer and a transition metal oxide layer was tested in Becerril-Romero (2019), in which a Mo:Na/V_2O_5/FTO back contact was used for CZTSSe-based solar cells, achieving 7.9% efficiency.

In the present work, solid solutions of $Cu_2ZnSn_{1-x}Ge_xSe_4$ (CZTGSe) thin films are deposited onto Mo/SLG and Mo/V_2O_5/FTO/glass substrates by thermal co-evaporation followed by a thermal treatment. A NaF precursor layer is deposited just before the kesterite co-evaporation in all the cases. It is demonstrated that the addition of Na promotes Ge-incorporation into the CZTSe lattice. The objective of this work is to study the influence of both, the Na as well as the type of back contact, on the structural, vibrational and compositional properties of the CZTGSe layer and the electronic characteristics of the corresponding solar cells.

2. Experimental section

2.1. Deposition of $Cu_2Zn(Sn,Ge)Se_4$ thin films

$Cu_2ZnSn_{1-x}Ge_xSe_4$ (CZTGSe) thin films were deposited onto 5 × 5 cm^2 Mo/soda-lime glass (SLG) and Mo/V_2O_5/FTO/glass substrates by co-evaporation of Cu, Sn, Ge, ZnSe and Se at a nominal substrate temperature of 150 °C. The low substrate temperature was used to minimize the losses of Sn and Ge. In this work, commercially available FTO with a sheet resistance of 7 Ω/sq and an optical transmission of 80–82% in the visible range has been used. In order to ensure a homogeneous film deposition, the substrate was rotating during the deposition process. A NaF layer was deposited at room temperature before the CZTGSe co-evaporation to compensate for the reduced Na diffusion from the SLG substrate towards the kesterite film during the low temperature deposition. The thickness of the NaF layer varied from 12 to 16 nm, in the case of using Mo/SLG substrates. As mentioned above, FTO blocks the Na diffusion coming from the SLG substrate (Caballero et al., 2006), thus it is necessary to evaporate a NaF precursor layer before the kesterite deposition. The co-evaporation process consisted of three stages. In the first stage, all elements were co-evaporated together. In the second stage, only Sn, Ge, ZnSe and Se were co-evaporated to ensure a final Cu-poor composition. To avoid a Zn-rich kesterite surface, Sn, Ge and Se were co-evaporated for 2 min in the final third stage. Using similar procedures, we deposited CZTSe and CZTGSe thin films, as previously reported in de la Cueva et al. (2018) and Ruiz-Perona et al. (2020). A 0.5 μm-Se capping layer was evaporated at room temperature in the same vacuum chamber to homogenize the kesterite surface and protect it against possible oxidation. As-deposited CZTGSe layers were then annealed in an Ar/Se-atmosphere using a two-stage process: 330 °C for 45 min and 480 °C for 15 min, as described in (Ruiz-Perona et al., 2020).

Table 1 summarizes the composition of CZTGSe thin films that were deposited using the same process parameters, with the only difference being in the thickness of the NaF-layer for Samples 1 and 2, and the type of the back contact configuration used for Samples 1 and 3. In order to reduce the series resistance that could lead to inefficient semi-transparent devices, a Mo (12 nm)/V_2O_5 (15 nm)/FTO/glass structure was used. In this work, a 12 nm NaF precursor layer was evaporated onto the Mo/V_2O_5/FTO/glass structure before CZTGSe co-evaporation (Sample 3 in Table 1). In addition to that, a reference CZTGSe sample has been added in Table 1. This Reference Sample was grown using the same conditions as for Samples 1 and 2, but without evaporating a NaF precursor layer (Ruiz-Perona et al., 2020).

2.2. Device fabrication

Solar cells were finished by chemical bath deposition of a CdS buffer layer (~50 nm) followed by pulsed DC-sputtering deposition of a transparent conductive window layer composed of i-ZnO (50 nm) and ITO (350 nm) layers. A KCN etching was performed before the CdS-deposition to clean and remove oxide phases from the surface of the absorber layer. Neither grids nor an antireflection coating were deposited onto the final solar cells devices. Furthermore, no thermal treatment was applied to the final photovoltaic devices.

2.3. Characterization techniques

Energy dispersive X-ray spectroscopy (EDX) (Oxford instruments, model INCAx-sight) using a Hitachi S-3000 N scanning electron microscope (SEM) was used to measure the chemical composition of the kesterite thin films. For that, an operating voltage of 25 kV and the Cu K, Zn K, Sn L, Ge K and Se K lines were used for elemental

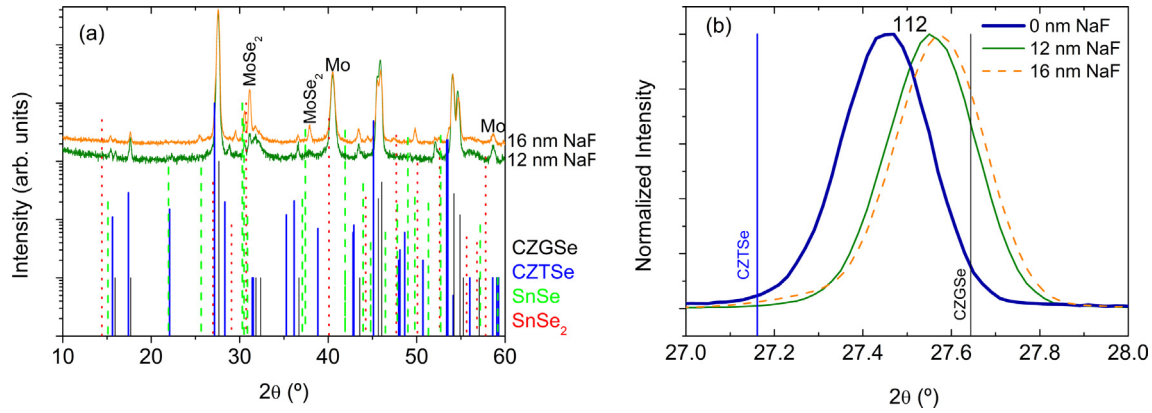

Fig. 1. (a) Grazing incidence (GI = 4°) X-ray diffraction spectra of Samples 1 and 2 and (b) 112 Bragg peak for the Reference Sample, Samples 1 and 2. The PDF data of $Cu_2ZnSnSe_4$ (blue thick solid lines), $Cu_2ZnGeSe_4$ (black solid lines), SnSe (green dotted lines) and $SnSe_2$ (red dashed lines) have been used for identification of the different phases.

quantification. The structural properties of the CZTGSe thin films were investigated by Grazing incidence X-ray diffraction (GIXRD) measurements. A PANAlytical ẊPert Pro MPD diffractometer, using Cu Kα radiation and a multilayer mirror to produce a parallel beam, were used to collect the GIXRD data. Detector scans with an incident angle of 4° were performed. The absorber surface was investigated by Raman spectroscopy done in a back-scattering configuration using the optical probe developed at IREC attached either to a FHR640 or an iHR320 monochromator, both coupled with low noise CCD detectors. In these systems, excitation and light collection were performed through a macro-optic system with a laser spot diameter of about 70 μm. The former monochromator is optimized for the ultraviolet and visible range, thus, the measurements were performed under 442 nm excitation wavelengths, while the second system is optimized for the near infrared (NIR) region and an excitation wavelength of 785 nm was used. The laser power density in both cases was ~80 W/cm^2. The first order Raman peak of monocrystalline Si at 520 cm^{-1} was used to correct the spectra. In order to ensure the lateral homogeneity of the surface, measurements of the kesterite layers were performed at different spots. In case of the 785 nm excitation, spectra from the front and from the back of the kesterite layer deposited onto semi-transparent substrates were analyzed.

The morphology of the CZTGSe/back contact/glass structure and the CZTGSe surface was studied by Scanning electron microscopy (*SEM*) using a Philips XL30S FEG scanning electron microscope, operating at 5 kV. The distribution of elements throughout the depth of the kesterite absorber layer was measured via glow discharge optical emission spectrometry (GD-OES) using a Spectruma GDA 650. Depth profiles are collected using an Argon plasma in a pulsed RF mode for sputtering and a CCD-array for the optical detection. Measurements were carried out after optimizing the sputtering parameters according to the procedure described in (Kodalle et al., 2019). The measurements were done without calibration samples, which is why the depth profiles are shown as qualitative plots. The depth profiles nevertheless give a reliable representation of the qualitative distribution of the containing elements in the kesterite layers, since all measurements were performed under the very same conditions. Transmittance of the kesterite/Mo/V_2O_5/FTO structure was measured with a Perkin Elmer lambda 950 spectrophotometer in a range from 300 to 1300 nm.

A Sun 3000 class solar simulator (Abet Technologies Inc., Milford, Connecticut, USA) was used to measure *I-V* characteristics of the solar cells under standard test conditions (25 °C, AM 1.5, 100 mW/cm^2). A Bentham PVE300 system (Bentham Instruments Ltd., Berkshire, UK) calibrated with Si and Ge photodiodes was used to measure the external quantum efficiency (*EQE*). In order to be able to collect reversed voltage-biased *EQE* curves, a Keithley 2400 source meter (Keithley Instruments Inc., Cleveland, Ohio, USA) was directly connected to the primary coil of the transformer and was used to bias the device at the desired voltage. Capacitance voltage measurements (*C-V*) were performed using a HP 4192A LF impedance analyzer at a frequency of 100 kHz and a small *ac* signal amplitude of 30 mV.

3. Results and discussion

3.1. Effect of Na concentration

As mentioned above, Neuschitzer et al. (2016) reported an interaction between Ge and Na in the Ge-doped CZTSe, which minimizes the loss of Sn and the formation of secondary phases, leading to an improvement of the solar cells' efficiency. In order to promote the incorporation of Ge into the kesterite lattice, solid solutions of CZTGSe thin films were grown onto Mo/SLG adding a NaF precursor layer. As it can be observed in Table 1, comparing the Reference Sample with Samples 1 and 2, the addition of more Na leads to a higher incorporation of Ge into the CZTSe lattice. In addition to that, a lower Cu content is also measured when more Na is added. The affinity of Na for V_{Cu} is well known, as for example in CIGSe solar cells (Caballero et al., 2013).

Fig. 1a shows GIXRD spectra (GI = 4°) of kesterite thin films with different composition. Literature data for tetragonal $Cu_2ZnSnSe_4$ (No. 04-010-6295), tetragonal $Cu_2ZnGeSe_4$ (No. 04-012-7580), SnSe (No. 04-009-2277) and $SnSe_2$ (No. 01-089-2939) have been used to identify the different phases. As it can be observed, the formation of the kesterite phase takes place in all samples. Moreover, the reflections corresponding to Mo and $MoSe_2$ are detected. The intensity of the $MoSe_2$ Bragg peaks is higher when more Na has been added. It is known from literature that a thicker NaF precursor film can lead to the formation of a thicker $MoSe_2$ film (Caballero et al., 2014). Furthermore, the XRD patterns reveal the presence of SnSe and $SnSe_2$ secondary phases. The presence of ZnSe and $Cu_2(Sn,Ge)Se_3$ phases cannot be ruled out since their diffraction peaks overlap with those of CZTGSe. The GIXRD spectrum of the Reference Sample was investigated previously (Ruiz-Perona et al., 2020), not showing any secondary phases. A small diffraction peak at around 52.1° is observed, which is difficult to assign to a unique phase. The diffraction peaks corresponding to Mo together with this peak can be observed for higher grazing incidence angles of 2° and 4°, not detecting it when using GI = 1° (not shown here). This fact is an indication that the phase attributed to this diffraction peak is present in the bulk or at the back side of the absorber layer. It has been reported the correlation of Na and O contents in CIGSe thin films (Ruckh et al., 1996), and more recently in kesterite thin films (Grini et al., 2019). The addition of a NaF precursor layer in CIGSe promotes

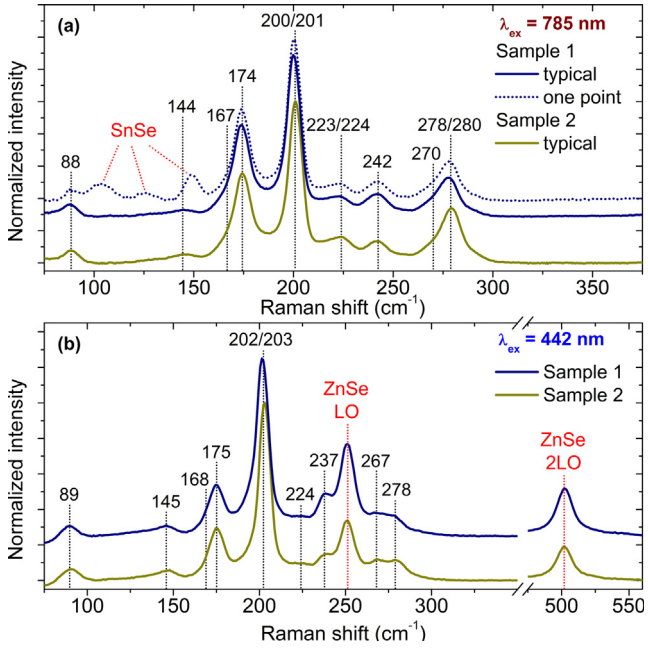

Fig. 2. Raman scattering spectra of Samples 1 and 2 measured under (a) 785 nm and (b) 442 nm excitation wavelengths. Here, the peaks attributed to secondary phases are indicated with the name of the corresponding secondary phase, while the peaks belonging to the CZTGSe phase are indicated with numbers corresponding to their position (Garcia-Llamas et al., 2017). The twin numbers are indicated in case there is a clear difference in peaks position between Sample 1 and 2.

not only the formation of $MoSe_2$, but also of MoO_3, as detected in Caballero et al. (2014). On the other hand, it cannot be ruled out that the diffraction peak in that range can be attributed to a Sn(Cu)-Se pseudobinary secondary phase. Further investigation is necessary to conclude about the phase attributed to this diffraction peak. Fig. 1b displays the 112-diffraction peak of the Reference Sample without NaF precursor layer as well as that of the Samples 1 and 2. The shift of the peak towards higher diffraction angles indicates the higher incorporation of Ge into the kesterite lattice by increasing the thickness of the NaF layer.

In order to evaluate the phase formation in the analyzed samples, Raman spectroscopy with different excitation wavelengths was applied. The blue (442 nm) excitation wavelength is used to detect the ZnSe phase (Fairbrother et al., 2014; Schorr et al., 2020), while the NIR laser (785 nm) can help to detect the SnSe, $SnSe_2$ and Cu_2SnSe_3 phases (Becerril-Romero et al., 2018; Schorr et al., 2020). Typical Raman spectra of the analyzed samples are presented in Fig. 2. It is confirmed that the kesterite phase is the main phase in all samples because it was observed the main Raman peaks of CZTGSe solid solutions in the spectra measured under both excitation wavelengths (Garcia-Llamas et al., 2017). The detection of intense A-like symmetry peaks and less intense E- and B-like symmetry peaks of the CZTGSe phase (Garcia-Llamas et al., 2017), and relatively low width of the peaks ($< 10\ cm^{-1}$ at the half maximum) denotes a good crystalline quality of the kesterite phase. The slight blue shift of the most intense CZTGSe Raman peak in Sample 2 can be explained by its higher Ge content as stated in Garcia-Llamas et al. (2017), in agreement with the EDX analysis. Moreover, comparison of the main CZTGSe peak position measured under NIR and blue excitation wavelength in both samples (200 and 202 cm^{-1}, respectively, for Sample 1; 201 and 203 cm^{-1}, respectively, for Sample 2) allows to conclude that the surface of the absorber layer is more Ge-rich than the bulk of the layer. This can be yielded from different penetration depths of the used excitation wavelengths following the logic that was previously described for anionic solid solutions of kesterite-type

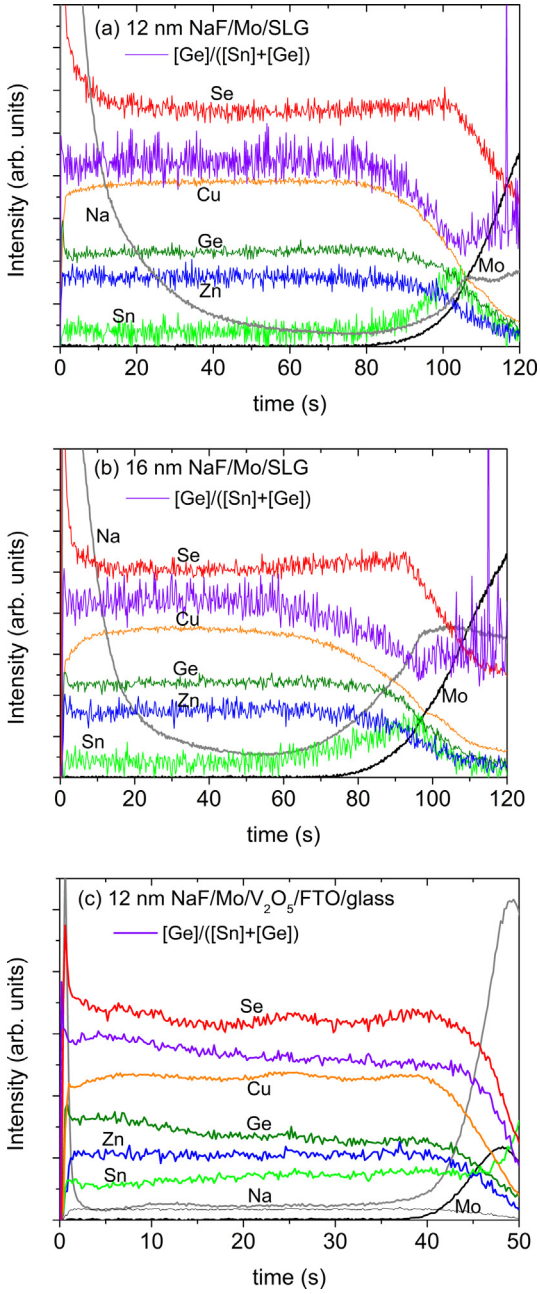

Fig. 3. GD-OES depth profiles of CZTGSe/Mo structure using (a) Samples 1 and (b) 2 as absorber layers. In (c) GD-OES depth profiles of CZTGSe/Mo/V_2O_5/FTO/glass structure are shown.

compounds (Andrade-Arvizu et al., 2019). In addition to the kesterite phase, the presence of a SnSe secondary phase was clearly detected in selected points of the surface of Sample 1, in agreement with the GIXRD measurements (see Fig. 2a), and the presence of a ZnSe secondary phase was detected in Sample 1 and 2 (see Fig. 2b). No ZnSe secondary phase was detected on the Reference Sample, as investigated previously in Ruiz-Perona et al. (2020).

Fig. 3a and b display GD-OES depth profiles of the elements through the absorber layer for Samples 1 and 2 deposited on Mo/SLG respectively. The Na-signal is higher close to the back contact and near the surface in both samples, which correlates with a lower Cu concentration at the surface and next to the Mo back contact. Moreover, the GD-OES profiles show a significantly higher Sn-signal near the Mo layer. Neuschitzer et al. (2016) proposed that, in kesterite with high amounts of Ge, Ge replaces Sn and the excess [Sn + Ge] can either occupy V_{Cu}

forming Sn_{Cu} and/or Ge_{Cu} deep donor defects, or induces the segregation of a secondary SnSe-phase as evidenced by GIXRD and Raman measurements. In this case, the accumulation of Sn near the Mo back contact may reaffirm that the small diffraction peak detected by GIXRD around 52.1° (see Fig. 1a) could be related to a Sn-Se or Cu-Sn-Se phase. A higher Se content is also observed near the Mo, in agreement with the formation of a $MoSe_2$ layer at the back interface as shown by GIXRD. Additionally, a sharp increase of Se and a slight increase of Ge and Zn signals are observed in the GD-OES signal at the absorber surface. Although one has to be careful interpreting the slight increase of Ge and Zn signals, they do agree with the results of the Raman study. Accordingly, the increase of the Ge-signal might be a hint for a higher Ge content at the surface of the solid solutions, while Zn and Se signal excess might correspond to the presence of ZnSe secondary phase also segregated at the surface of the absorber layer, both effects are observed in the Raman analysis. The depth profile of the [Ge]/([Sn] + [Ge])-atomic ratio is also plotted. A very uniform distribution of the atomic ratio is observed from the absorber surface until the region near the back contact, where this ratio decreased significatively because of the increased Sn content. Previously, we investigated the distribution of the elements for the Reference Sample by Auger Electron Spectroscopy (AES) depth profiles through Mo/CZTGSe/CdS/ZnO/ITO device. A very uniform distribution of Cu, Zn, Sn, Ge and [Ge]/([Sn] + [Ge]) atomic ratio was measured. A higher Se content near the Mo back contact was detected and related to the formation of $MoSe_2$ phase at the back interface, as corroborated by in-depth Raman spectroscopy measurements (Ruiz-Perona et al., 2020). However, the $MoSe_2$ phase was not detected by GIXRD measurements, indicating that the lower is the Na concentration, the less is the presence of $MoSe_2$ at the CZTGSe/Mo interface.

Fig. 4 shows the cross-sectional SEM images of the kesterite/Mo/SLG structure corresponding to Samples 1 and 2. Bigger kesterite grain size is observed when more Na has been added, in accordance with the results reported in literature (Romnayuk et al., 2019). Both absorber layers present a compact structure. Despite using the same experimental conditions to grow Samples 1 and 2, the CZTGSe-layer grown with a smaller amount of Na, 12 nm NaF, is slightly thicker, 1.36 μm, than the absorber that was grown with 16 nm NaF (1.21 μm).

The photovoltaic (PV) parameters of the best devices are displayed in Table 2. *EQE* spectra of the solar cells shown in Table 2, and measured at 0 V and under a reverse bias of −1 V, are plotted in Fig. 5. A higher collection in the whole range of wavelengths with negative bias (-1 V) is observed for all the devices. The increased collection for the long wavelength range under applying reverse-bias voltage indicates a poor collection of electrons generated deeper in the bulk of the absorber layer (Scheer and Schock, 2011). The optical band gap energy was determined from the inflection point of the *EQE* spectra at long wavelengths. The Device 1 with lower Ge-content leads to a higher spectral response in the infrared range, which results in higher J_{SC} and lower E_g. A band-gap energy E_g of 1.30 and 1.34 eV, and V_{OC}-deficit of 775 and 842 mV have been determined for Devices 1 and 2 respectively. A similar increase of the V_{OC}-deficit with the bandgap energy was reported previously for CZTGSe-based devices (Kim et al., 2016). However, this effect cannot be the only reason of the higher V_{OC}-deficit (40 meV of E_g increase versus 67 mV of V_{OC}-deficit increase), which suggests the presence of a detrimental effect of Na-excess in the absorber layer on the electronic properties of the device. As shown in Table 1, samples with higher Na content also present lower Cu concentration (comparison between Samples 1 and 2 for CZTGSe), which may result in a higher presence of detrimental Sn_{Cu} and/or Ge_{Cu} deep donor defects reducing the *p*-type conductivity and/or increasing the recombination loss in the device. On the other hand, all the absorber layers were characterized by the presence of secondary phases on the surface. Therefore, despite using the same experimental conditions to deposit the CdS buffer and window layer for all the devices, the surface of each absorber was different, which could significantly influence the hetero-interface of the devices

The highest efficiencies were obtained for solar cells based on CZTGSe with 12 nm NaF, achieving $\eta = 4.7\%$. However, this value is still lower than that obtained with the Reference Sample. The performance of Device 1 is mainly limited by its low *FF*. Sn-Se phases are present at the surface as determined by Raman spectroscopy, but also in the bulk of the CZTGSe layer as evidenced by GIXRD (GI = 4°). The presence of these phases together with ZnSe can be one of the reasons of the limited efficiency. Moreover, a comparison of the relative intensity of the ZnSe Raman peak measured on Device 1 with the one measured on a series of solar cells with different ZnSe content presented in a previous study (Ruiz-Perona et al., 2020), suggests that the maximum efficiency of the devices with a similar amount of the ZnSe phase is around 4.6%, which is comparable to the one measured in the present work. This denotes the insignificant influence of a small amount of additional Na to the device performance, while its increase leads to the worsening of solar cells efficiency.

Fig. 6 displays the dependence of the charge carrier concentration on width of the depletion region as measured by capacitance-voltage profiling. The depletion width (w_d) of the devices at a bias voltage of 0 V is approximately 0.53 and 0.33 μm, respectively, and a carrier concentration N_{CV} of 3.6×10^{15} and 1.2×10^{16} cm^{-3} can be extracted for Devices 1 and 2, respectively. An increased carrier concentration and shorter depletion width is obtained for solar cells with higher Na content. The decreased w_d for the device with 16 nm NaF is consistent with the lowest J_{SC}. However, the higher carrier concentration does not lead to an enhanced V_{OC} despite a higher E_g indicating that the incorporation of more NaF increases the recombination rate in the device. Another effect contributing to the rather low J_{SC} and *FF* of Device 2 is its high series resistance (R_s), which might originate from the higher amount of secondary phases in this sample as well.

3.2. Influence of the back contact

The CZTGSe thin film on a semi-transparent substrate was deposited following the same experimental procedure as used for Sample 1 with a

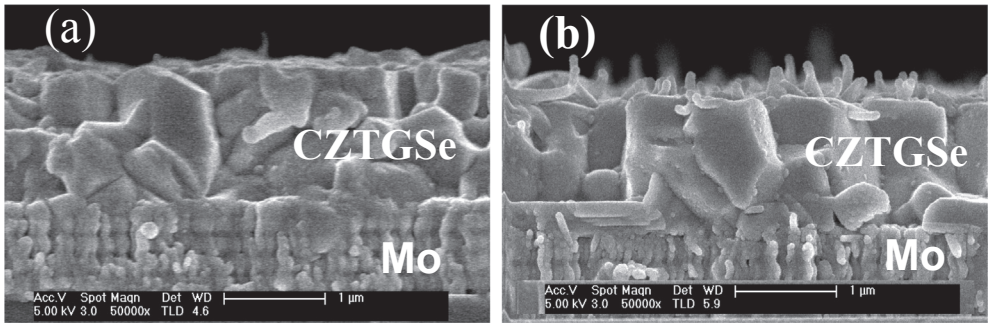

Fig. 4. Cross-sectional SEM micrographs of CZTGSe/Mo structure using (a) Samples 1 and (b) 2 as absorber layers.

Table 2
Photovoltaic parameters, bandgap energy and V_{OC}-deficit of CZTGSe solar cells.

Sample	NaF (nm)	V_{OC} (mV)	J_{SC} (mA/cm^2)	*FF* (%)	η (%)	R_s (Ωcm^2)	R_p (Ωcm^2)	E_g (eV)	E_g/q-V_{OC} (mV)
Ref.	0	510	22.4	56.3	6.4	3.7	239.6	1.28	770
1	12	515	20.2	44.8	4.7	3.4	102.8	1.30	775
2	16	498	19.3	41.6	4.0	5.1	109.4	1.34	842
3	12	503	21.0	53.2	5.6	3.1	115.7	1.28	777

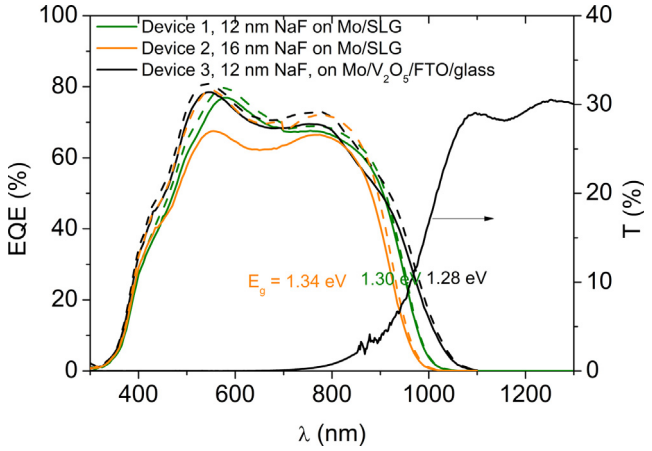

Fig. 5. Unbiased and reverse bias *EQE* curves of all the devices investigated. Transmittance spectra of CZTGSe/Mo/V_2O_5/FTO/glass structure is also plotted.

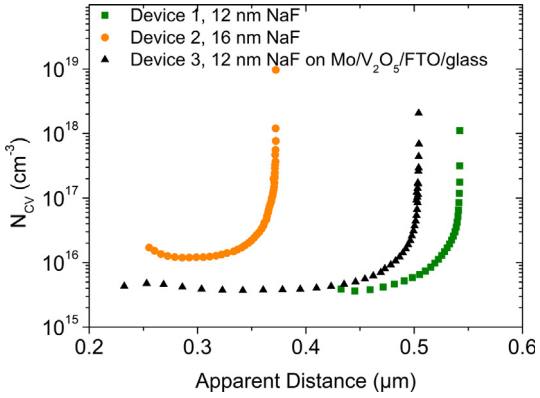

Fig. 6. Capacitance-Voltage (*C-V*) spectra of Devices 1, 2 and 3 measured at 10^5 Hz.

12 nm thick NaF precursor layer, which produces a reduced V_{OC}-deficit and higher performance compared to the sample with a 16 nm thick NaF-layer. Fig. 7a shows the GIXRD spectrum of CZTGSe thin films grown on the Mo/V_2O_5/FTO/glass structure (Sample 3). Kesterite is identified as the main phase together with diffraction reflections corresponding to the FTO back contact. The formation of the CZTGSe solid solution was also confirmed by Raman scattering. No peaks related to secondary phases were detected at the absorber surface in the spectra measured under 442 and 785 nm excitation wavelengths (see examples of the spectra in Fig. 7b and c). Moreover, the use of the semi-transparent back contact allows measuring Raman spectra at the back of the CZTGSe absorber layer under 785 nm excitation. This allowed to follow up the formation of a CZTGSe solid solution in depth of the absorber and to detect a slight decrease of the [Ge]/([Ge] + [Sn]) atomic ratio from the surface to the back of the absorber (the position of the main peak shift from 200 to 201 cm^{-1} from the back towards the front of absorber (Fig. 7b)). The presence of the $MoSe_2$ peaks was also detected in the spectra measured at the back of the absorber. This result shows that 12 nm of Mo deposited on V_2O_5/FTO/glass is enough to form

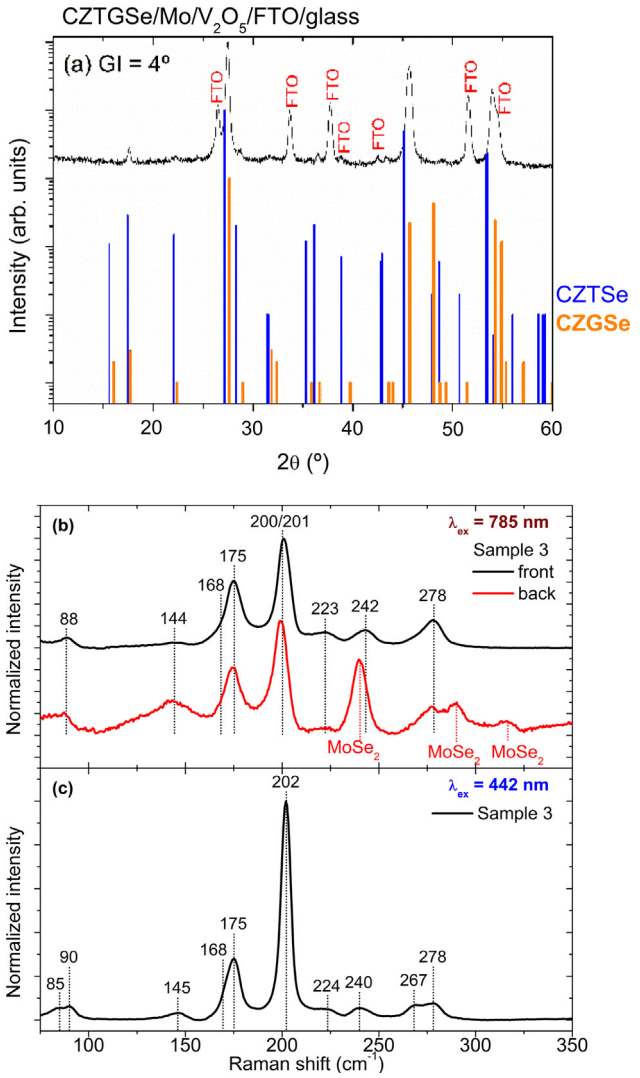

Fig. 7. (a) GIXRD (GI = 4°) diffractogram of CZTGSe thin films deposited on Mo/V_2O_5/FTO/glass. The PDF data of $Cu_2ZnSnSe_4$ (blue thick solid lines) and $Cu_2ZnGeSe_4$ (orange thick solid lines) have been used for the identification of the different phases. (b and c) Raman scattering spectra of the same sample measured under 785 nm and 442 nm excitation wavelength. Here, the peaks of the $MoSe_2$ phase are indicated with red dotted lines, while the rest of the peaks, indicated with the numbers corresponding to their positions, belong to the CZTGSe phase (Garcia-Llamas et al., 2017). The twin number is indicated for the peak with a clear difference in position between back and front spectra.

$MoSe_2$ at the back interface of the absorber.

Fig. 8a and b show the surface of the absorber layer and the cross-sectional SEM pictures of the CZTGSe/Mo/V_2O_5/FTO/glass structure respectively. This absorber layer of 0.95 μm of thickness is characterized by a big grain size and columnar and dense morphology, similar to the results observed when deposited onto Mo/SLG. However, CZTGSe on the semi-transparent back contact is thinner than that deposited following the same conditions on Mo/SLG. The growth of CZTGSe

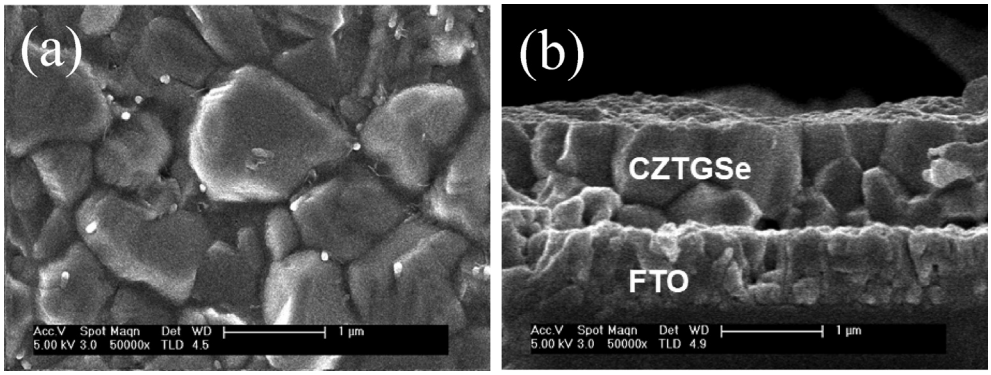

Fig. 8. (a) Surface and (b) cross-sectional SEM micrographs of CZTGSe thin films deposited on Mo/V_2O_5/FTO/glass.

depends on the substrate used, which can therefore also affect the thickness of the absorber layer.

GD-OES depth profiles of the elemental distribution are displayed in Fig. 3c. A more uniform distribution of Sn through the kesterite layer is observed in this sample compared to the absorbers grown on Mo/SLG, in agreement with the lack of Sn-Se secondary phases. A slightly decreased Sn-signal is detected at the surface. The opposite trend is measured for the Ge-distribution, confirming the slight gradient of the [Ge]/([Ge] + [Sn]) ratio in depth of the absorber in agreement with the Raman analysis (cf. the main peak position in Fig. 7b and c). The higher Sn-signal near the back contact is due to the FTO layer used. The fact that the Cu-signal rapidly decreases at the back interface, while the Se-signal maintains deeper in the layer, can be related to the formation of a $MoSe_2$ layer as detected by Raman spectroscopy. However, this increase of the Se content next to the back contact is not as pronounced as those observed in the kesterite layers deposited onto Mo/SLG, suggesting the formation of a thinner $MoSe_2$ layer on the semi-transparent substrates due to the limited availability of Mo.

Solar cell devices are fabricated using the ITO/i-ZnO/CdS/CZTGSe/Mo/V_2O_5/FTO/glass structure (see Table 2), achieving a maximum efficiency of 5.6% and a V_{OC}-deficit of 777 mV, the same deficit as for Device 1. The enhanced device performance in comparison to Sample 1 when using a semi-transparent substrate is mainly due to a higher *FF*. Using a semi-transparent back contact, neither Sn-Se secondary phases nor a ZnSe-phase have been formed as determined by GIXRD and Raman spectroscopy, which could be the origin of the enhanced *FF*. The series resistance of Device 3 is in the same range as that obtained for Device 1 on Mo/SLG. This shows the good role of the Mo/V_2O_5 bilayer deposited onto FTO/glass substrate. As detected by Raman spectroscopy, a $MoSe_2$ layer has been formed at the CZTGSe/Mo interface despite the thinner Mo layer and lower Na content. As mentioned before, the $MoSe_2$ phase was also identified for the absorbers grown on Mo/SLG, as shown in Fig. 1. There are two sources that supply Na to the kesterite layers when those are deposited onto Mo/SLG: by diffusing Na from the SLG substrate and the the use of a NaF precursor layer. Therefore, a higher Na content is expected for these cases in comparison to the kesterite grown on FTO, which is supported by the GD-OES measurements. As reported previously, Na acts as catalyst that enhances the formation of a $MoSe_2$ layer at the back interface of the devices (Caballero et al., 2014). However, a too thick $MoSe_2$ layer, developed in part by a higher Na concentration, can produce a worse back contact that can lead to a deterioration of the solar cell efficiency. As shown in Table 2, the Device 2 with the thicker NaF layer and with Mo/SLG substrate presents the lowest PV parameters and also the highest intensity of the $MoSe_2$ Bragg peaks in the GIXRD spectra (see Fig. 1). Not only the amount of Na supplied, but also the use of a different back contact configuration could lead to a different alignment of $MoSe_2$ that would result in a different series resistance explaining the effect on the PV parameters (Würz et al., 2003; Caballero et al., 2010), especially *FF* and J_{SC} of the solar cells. Fig. 5 displays *EQE* spectra at 0 V and under reverse bias (-1 V) of the best solar cell on FTO together with the transmittance spectra of the CZTGSe on this back contact structure. A transmission of 30% is achieved in the near infrared range for the FTO-cell, being a promising starting point for its use in semi-transparent solar cells. A poorer carrier collection is again detected in the long wavelength region. As shown in Fig. 6, the depletion width (w_d) in Device 3 at a bias voltage of 0 V is approximately 0.47 µm and its carrier concentration is $N_{CV} = 7.7 \times 10^{15}$ cm^{-3}. Although Device 3 presents a lower Na concentration, a higher carrier concentration is measured compared to Device 1. This indicates that the Na content is not the only responsible parameter for the increased N_{CV}. The use of another back contact and different elemental distributions make it difficult to separate the different factors that can alter the carrier concentration and in consequence the width of the depletion region. As mentioned above, a different Ge distribution was measured for Sample 3 in comparison to Samples 1 and 2. The Ga double-grading through the absorber layer has been one of the key parameters to enhance the efficiency of CIGSe-based devices (Witte et al., 2015). We believe that an optimization of the Ge-gradient through CZTGSe layer can be a key point to increase the solar cells performance. Here, a single-[Ge]/([Ge] + [Sn]) gradient is formed, continually increasing from the back towards the absorber surface, for Sample 3. However, a pretty uniform distribution of this atomic ratio is observed for Samples 1 and 2, but with an abrupt decrease of the [Ge]/([Ge] + [Sn]) ratio near the back contact. An increased of Ge concentration or [Ge]/([Ge] + [Sn])-atomic ratio near the back contact would help to enhance the carrier collection, by generating a back surface field and reducing the recombination at the back interface. The opposite behavior is obtained for Samples 1 and 2 because of the increased Sn content near the Mo layer, which resulted in lower J_{sc}. Therefore, the absence of secondary phases and the Ge-gradient for Sample 3 probably allows for a better heterojunction that enhances the device efficiency.

4. Conclusions

CZTGSe thin films have been fabricated by co-evaporation at 150 °C and a subsequent annealing in Se-atmosphere at 480 °C. A NaF precursor layer was deposited before the CZTGSe co-evaporation process. It was shown that a higher Na content produces larger kesterite grain size, higher carrier concentration and shorter space charge region. But more importantly, the promotion of the incorporation of Ge into the CZTSe lattice via the addition of Na has been demonstrated. By this way, CZTGSe thin films with $E_g = 1.30$ and 1.34 eV as well as efficiencies of $\eta = 4.7$ and 4.0% have been achieved by using 12 nm and 16 nm NaF precursor layers respectively. CZTGSe grown on Mo/SLG were characterized by the presence of Sn-Se and ZnSe secondary phases, which are proposed to be the main limitations for the device efficiency. Furthermore, ITO/i-ZnO/CdS/CZTGSe/NaF/Mo/V_2O_5/FTO/glass solar cells with an efficiency of 5.6%, $E_g = 1.28$ eV and transmittance of 30% in the near infrared were obtained. The absence of

secondary phases, the formation of only a thin layer of $MoSe_2$ at the back interface and the Ge-gradient through the absorber layer could be responsible for the increased efficiency in these semi-transparent photovoltaic devices.

Declaration of Competing Interest

The authors declare that they have no known competing financial interests or personal relationships that could have appeared to influence the work reported in this paper.

Acknowledgements

This work was supported by Spanish Ministry of Science, Innovation and Universities Project (WINCOST, ENE2016-80788-C5-2-R) and European Project INFINITE-CELL (H2020-MSCA-RISE-2017-777968). ARP also acknowledges financial support from Community of Madrid within Youth Employment Program (PEJD-2017-PRE/IND-4062). MG acknowledges the financial support from ACCIÓ-Generalitat de Catalunya within the TECNIOspring Plus fellowship (TECSPR18-1-0048). MP acknowledges the financial support from Spanish Ministry of Science, Innovation and Universities within the Ramón y Cajal Program (RYC-2017-23758). The authors would like to thank K. Mayer-Stillrich and M. Hartig at PVComB-HZB for Mo deposition, Dr. G. San Vicente from CIEMAT for allowing to perform transmittance mesaurements, Prof. Dr. F. Briones from Instituto de Micro y Nanotecnología, CSIC, and Dr. I. Fernández from Nano4Energy for the technical support with the Se evaporation source.

Appendix A. Supplementary material

Supplementary data to this article can be found online at https://doi.org/10.1016/j.solener.2020.06.044.

References

Abzieher, T., Schnabel, T., Hetterich, M., Powalla, M., Ahlswede, E., 2016. Source and effects of sodium in solution-processed kesterite solar cells. Phys. Status Solidi A 213, 1039–1049. https://doi.org/10.1002/pssa.201532619.

Almora, O., Gerling, L.G., Voz, C., Alcubilla, R., Puigdollers, J., Garcia-Belmonte, G., 2017. Superior performance of V_2O_5 as hole selective contact over other transition metal oxides in silicon heterojunction solar cells. Sol. Energy Mater. Sol. Cells 168, 221–226. https://doi.org/10.1016/j.solmat.2017.04.042.

Andrade-Arvizu, J., Izquierdo-Roca, V., Becerril-Romero, I., Vidal-Fuentes, P., Fonoll-Rubio, R., Sánchez, Y., Placidi, M., Calvo-Barrio, L., Vigil-Galán, O., Saucedo, E., 2019. Is it possible to develop complex S-Se graded band gap profiles in Kesterite-based solar cells? ACS Appl. Mater. Interfaces 11, 32945–32956. https://doi.org/10.1021/acsami.9b09813.

Andres, C., Schwarz, T., Haass, S., Weiss, T., Carron, R., Caballero, R., Figi, R., Schreiner, C., Bürki, M., Tiwari, A.N., Romanyuk, Y.E., 2018. Decoupling of optoelectronic properties from morphological changes in sodium treated kesterite thin film solar cells. Solar Energy 175, 94–100. https://doi.org/10.1016/j.solener.2018.03.067.

Becerril-Romero, I., 2019. Alternative substrates for sustainable and earth-abundant thin film photovoltaics. PhD thesis. Universitat de Barcelona.

Becerril-Romero I., Acebo L., Oliva F., Izquierdo-Roca V., López-Marino S., Espíndola-Rodríguez M.,| Neuschitzer M., Sánchez Y., Placidi M., Pérez-Rodríguez A., Saucedo E., Pistor P., 2018. CZTSe solar cells developed on polymer substrates: Effects of low temperature processing. Prog. Photovolt. Res. Appl. 26, 55–68. DOI: 10.1002/pip.2945.

Caballero, R., Siebentritt, S., Sakurai, K., Kaufmann, C.A., Lux-Steiner, M.Ch., 2006. CGS-thin films solar cells on transparent back contact. In: 2006 IEEE 4th World Conference on Photovoltaic Energy, vol. 1, pp. 479–482.

Caballero, R., Kaufmann, C.A., Eisenbarth, T., Grimm, A., Lauermann, I., Unold, T., Klenk, R., Schock, H.W., 2010. Influence of Na on Cu(In, Ga)S_e2 solar cells grown on polyimide substrates at low temperature: Impact on the Cu(In, Ga)$_S$e2/Mo interface. Appl. Phys. Lett. 96, 092104. https://doi.org/10.1063/1.3340459.

Caballero, R., Kaufmann, C.A., Efimova, V., Rissom, T., Hoffmann, V., Schock, H.W., 2013. Investigation of Cu(In, Ga)S_e2 thin-film formation during the multi-stage co-evaporation process. Progr. Photovolt : Res. Appl. 21, 30–46. https://doi.org/10.1002/pip.1233.

Caballero, R., Nichterwitz, M., Steigert, A., Eicke, A., Lauermann, I., Schock, H.W., Kaufmann, C.A., 2014. Impact of Na on $MoSe_2$ formation at the CIGSe/Mo interface in thin-film solar cells on polyimide foil at low process temperatures. Acta Mater. 63, 54–62. https://doi.org/10.1016/j.actamat.2013.09.051.

de la Cueva, L., Sánchez, Y., Calvo-Barrio, L., Oliva, F., Izquierdo-Roca, V., Khelifi, S., Bertram, T., Merino, J.M., León, M., Caballero, R., 2018. Sulfurization of co-evaporated $Cu_2ZnSnSe_4$ thin film solar cells: the role of Na. Sol. Energy Mater. Sol. Cells 186, 115–123. https://doi.org/10.1016/j.solmat.2018.06.015.

Espíndola-Rodríguez, M., Sylla, D., Sánchez, Y., Oliva, F., Grini, S., Neuschitzer, M., Vines, L., Izquierdo-Roca, V., Saucedo, E., Placidi, M., 2017. Bifacial kesterite solar cells on FTO substrates. ACS Sustain. Chem. Eng. 5, 11516–11524. https://doi.org/10.1021/acssuschemeng.7b02797.

Fairbrother, A., Fontané, X., Izquierdo-Roca, V., Placidi, M., Sylla, D., Espindola-Rodriguez, M., López-Mariño, S., Pulgarín, F.A., Vigil-Galán, O., Pérez-Rodríguez, A., Saucedo, E., 2014. Secondary phase formation in Zn-rich $Cu_2ZnSnSe_4$-based solar cells annealed in low pressure and temperature conditions. Prog. Photovolt: Res. Appl. 22, 479–487. https://doi.org/10.1002/pip.2473.

Garcia-Llamas, E., Guc, M., Bodnar, I.V., Fontané, X., Caballero, R., Merino, J.M., León, M., Izquierdo-Roca, V., 2017. Multiwavelength excitation Raman scattering of $Cu_2ZnSn_{1-x}Ge_x$(S, Se)4 single crystals for earth abundant photovoltaic applications. J. Alloys Comp. 692, 249–256. https://doi.org/10.1016/j.jallcom.2016.09.035.

Ge, J., Ghu, J., Jiang, J., Yan, Y., Yang, P., 2015. The interfacial reaction at ITO back contact in kesterite CZTSSe bifacial solar cells. ACS Sustain. Chem. Eng. 3, 3043–3052. https://doi.org/10.1021/acssuschemeng.5b00962.

Giraldo, S., Jehl, Z., Placidi, M., Izquierdo-Roca, V., Pérez-Rodríguez, A., Saucedo, E., 2019. Progress and perspectives of thin film kesterite photovoltaic technology: a critical review. Adv. Mater. 31, 1806692. https://doi.org/10.1002/adma.201806692.

Grini, S., Sopiha, K.V., Ross, N., Liu, X., Bjørheim, T.S., Platzer-Björkman, C., Persson, C., Vines, L., 2019. Strong interplay between sodium and oxygen in kesterite absorbers: complex formation, incorporation and tailoring depth distributions. Adv. Energy Mater. 9, 1900740. https://doi.org/10.1002/aenm.201900740.

Kim, S., Kim, K.M., Tampo, H., Shibata, H., Matsubara, K., Niki, S., 2016. Ge-incorporated $Cu_2ZnSnSe_4$ thin-film solar cells with efficiency greater than 10%. Sol. Energy Mater. Sol. Cells 144, 488–492. https://doi.org/10.1016/j.solmat.2015.09.039.

Kodalle, T., Greiner, D., Brackmann, V., Prietzel, K., Scheu, A., Bertram, T., Reyes-, Figueroa P., Unold, T., Abou-Ras, D., Schlatmann, R., Kaufmann, C.A., Hoffmann, V., 2019. Glow discharge optical emission spectrometry for quantitative depth profiling of CIGSe thin-films. J. Anal. At. Spectrom. 34, 1233–1241. https://doi.org/10.1039/C9JA00075E.

Li, J.V., Kuciauskas, D., Young, M.R., Repins, I.L., 2013. Effects of sodium incorporation in co-evaporated $Cu_2ZnSnSe_4$ thin-film solar cells. Appl. Phys. Lett. 102, 163905. https://doi.org/10.1063/1.4802972.

Liu, L., Lau, T.K., Zhi, Z., Huang, L., Wang, S., Xiao, X., 2018. Modification of Mo back contact with MoO_{3-x} layer and its effect to enhance the performance of Cu_2ZnSnS_4 solar cells. Sol. RRL 2, 1800243. https://doi.org/10.1002/solr.201800243.

López-Marino, S., Espíndola-Rodríguez, M., Sánchez, Y., Alcobé, X., Oliva, F., Xie, H., Neutschitzer, M., Giraldo, S., Placidi, M., Caballero, R., Izquierdo-Roca, V., Pérez-Rodríguez, A., Saucedo, E., 2016. The importance of back contact modification in $Cu_2ZnSnSe_4$ solar cells: the role of a thin MoO_2 layer. Nano Energy 26, 708–721. https://doi.org/10.1016/j.nanoen.2016.06.034.

Neuschitzer, M., Marquez, J., Giraldo, S., Dimitrievska, M., Placidi, M., Forbes, I., Izquierdo-Roca, V., Pérez-Rodríguez, A., Saucedo, E., 2016. V_{oc} boosting and grain growth enhancing Ge-doping strategy for $Cu_2ZnSnSe_4$ photovoltaic absorbers. J. Phys. Chem. C 120, 9661–9670. https://doi.org/10.1021/acs.jpcc.6b02315.

Platzer-Björkman, C., Frisk, C., Larsen, J.K., Ericson, T., Li, S.Y., Scragg, J.J.S., Keller, J., Larsson, F., Törndahl, T., 2015. Reduced interface recombination in Cu_2ZnSnS_4 solar cells with atomic layer deposition $Zn_{1-x}Sn_xO_y$ buffer layers. Appl. Phys. Lett. 107, 243904. https://doi.org/10.1063/1.4937998.

Repins, I., Beall, C., Vora, N., DeHart, C., Kuciauskas, D., Dippo, P., To, B., Mann, J., Hsu, W.-C., Goodrich, A., Noufi, R., 2012. Co-evaporated $Cu_2ZnSnSe_4$ films and devices. Sol. Energy Mater. Sol. Cells 101, 154–159. https://doi.org/10.1016/j.solmat.2012.01.008.

Romnayuk, Y.E., Haass, S.G., Giraldo, S., Placidi, M., Tiwari, D., Fermin, D.J., Hao, X., Xin, H., Schnabel, T., Kauk-Kuusik, M., Pistor, P., Lie, S., Wong, L.H., 2019. Doping and alloying of kesterites. J. Phys. Energy 1, 044004. https://doi.org/10.1088/2515-7655/ab23bc.

Ruckh, M., Schmid, D., Kaiser, M., Schäffeler, R., Walter, T., Schock, H.W., 1996. Influence of substrates on the electrical properties of Cu(In, GA)Se2 thin films. Solar Energy Mater. Solar Cells 41–42, 335–343. https://doi.org/10.1016/0927-0248(95)00105-0.

Ruiz-Perona, A., Sánchez, Y., Guc, M., Calvo-Barrio, L., Jawhari, T., Merino, J.M., León, M., Caballero, R., 2020. Influence of Zn excess on compositional, structural and vibrational properties of $Cu_2ZnSn_{0.5}Ge_{0.5}Se_4$ thin films and their effect on solar cell efficiency. Solar Energy 199, 864–871. https://doi.org/10.1016/j.solener.2020.02.082.

Scheer, R., Schock, H.W., 2011. Chalcogenide Photovoltaics. Wiley-VCH Verlag, Weinheim, Germany.

Schorr, S., Gurieva, G., Guc, M., Dimitrievska, M., Pérez-Rodríguez, A., Izquierdo-Roca, V., Schnohr, C.S., Kim, J., Jo, W., Merino, J.M., 2020. Point defects, compositional fluctuations and secondary phases in non-stoichiometric kesterites. J. Phys. Energy 2, 012002. https://doi.org/10.1088/2515-7655/ab4a25.

Son, D.-H., Kim, S.-H., Kim, S.-Y., Kim, Y.-I., Sim, J.-H., Park, S.-N., Jeon, D.-H., Hwang, D.-K., Sung, S.-J., Kang, J.-K., Yang, K.-J., Kim, D.-H., 2019. Effect of solid-H_2S gas reactions on CZTSSe thin film growth and photovoltaic properties of a 12.62% efficiency device. J. Mater. Chem. A 7, 25279–25289. https://doi.org/10.1039/C9TA08310C.

Sutter-Fella, C.M., Stückelberger, J.A., Hagendorfer, H., Mattina, F.L., Kranz, L., Nishiwaki, S., Uhl, A.R., Romanyuk, Y.E., Tiwari, A.N., 2014. Sodium assisted sintering of chalcogenides and its application to solution processed Cu_2ZnSn(S, Se)4 thin

film solar cells. Chem. Mater. 26, 1420–1425. https://doi.org/10.1021/cm403504u.
Temgoua, S., Bodeux, R., Mollica, F., Naghavi, N., 2019. Comparative study of $Cu_2ZnSnSe_4$ solar cells grown on transparent conductive oxides and molybdenum substrates. Solar Energy 194, 121–127. https://doi.org/10.1016/j.solener.2019.10.050.
Wang, W., Winkler, M.T., Gunawan, O., Gokmen, T., Todorov, T.K., Zhu, Y., Mitzi, D.B., 2014. Device characteristics of CZTSSe thin-film solar cells with 12.6% efficiency. Adv. Energy Mater. 4, 1301465. https://doi.org/10.1002/aenm.201301465.
Witte, W., Abou-Ras, D., Albe, K., Bauer, G.H., Bertram, F., Boit, C., Brügemann, R., Christen, J., Dietrich, J., Eicke, A., Hariskos, D., Maiberg, M., Mainz, R., Meessen, M., Müller, M., Neumann, O., Orgis, T., Paetell, S., Pohl, J., Rodríguez-Álvarez, H., Scheer, R., Schock, H.-W., Unold, T., Weber, A., Powalla, M., 2015. Gallium gradients in Cu(In, Ga)S_e2 thin-film solar cells. Prog. Photovolt: Res. Appl. 23, 717–733. https://doi.org/10.1002/pip.2485.
Würz, R., Fuentes-Marrón, D., Meeder, A., Rumberg, S., Babu, S.M., Schedel-Niedrig, T., Bloeck, U., Shcubert-Bischoff, P., Lux-Steiner, M.Ch., 2003. Thin Solid Films 431–432, 398–402.
Xie, H., López-Marino, S., Olar, T., Sánchez, Y., Neuschitzer, M., Oliva, F., Giraldo, S., Izquierdo-Roca, V., Lauermann, I., Pérez-Rodríguez, A., Saucedo, E., 2016. Impact of Na dynamics at the $Cu_2ZnSn(S, Se_)4$/CdS interface during post low temperature treatment of absorbers. Appl. Mater. Interfaces 8, 5017–5024. https://doi.org/10.1021/acsami.5b12243.